Small Structures

small structures

www.small-structures.com

RESEARCH ARTICLE OPEN ACCESS

Bottom-Up Synthesized B_3N_3-Doped Amorphous Carbon Monolayer

Birce Sena Tömekçe[1] | Vladimir Calvi[2,3] | Diego Jaramillo[4] | Hang Sik Kim[5] | Hyeongjoon Kim[6,7] | Daniele Poletto[8] | Vivek Chandrakant Wakchaure[8] | Matthew David Barnes[3] | Michele Buscema[3] | Sorin Melinte[4] | Young-Min Kim[5,6] | Hyeon Suk Shin[6,9,10] | Davide Bonifazi[8] | Richard van Rijn[3] | Irene M. N. Groot[2] | Willi Auwärter[1]

[1]Physics Department E20, TUM School of Natural Sciences, Technical University of Munich, Garching, Germany | [2]Leiden Institute of Chemistry, Leiden University, Leiden, The Netherlands | [3]Applied Nanolayers B.V., Delft, Netherlands | [4]Institute of Information and Communication Technologies, Electronics and Applied Mathematics (ICTEAM), Université catholique de Louvain, Louvain-la-Neuve, Belgium | [5]Department of Energy Science, Sungkyunkwan University (SKKU), Suwon, Republic of Korea | [6]Center for 2D Quantum Heterostructures, Institute for Basic Science (IBS), Suwon, Republic of Korea | [7]Department of Chemistry, Ulsan National Institute of Science and Technology (UNIST), Ulsan, Republic of Korea | [8]Institute of Organic Chemistry, Faculty of Chemistry, University of Vienna, Wien, Austria | [9]Department of Chemistry, Sungkyunkwan University (SKKU), Suwon, Republic of Korea | [10]Department of Energy, Sungkyunkwan University (SKKU), Suwon, Republic of Korea

Correspondence: Davide Bonifazi (davide.bonifazi@univie.ac.at) | Irene M. N. Groot (i.m.n.groot@lic.leidenuniv.nl) | Willi Auwärter (wau@tum.de)

Received: 15 October 2025 | **Revised:** 16 December 2025 | **Accepted:** 24 December 2025

Keywords: amorphous carbon monolayer | atomic force microscopy | B_3N_3-doping | borazine | electron microscopy | material transfer | Raman spectroscopy | scanning tunneling microscopy | surface-assisted synthesis | X-ray photoelectron spectroscopy

ABSTRACT

Research on amorphous carbon monolayers (ACMs) has accelerated in recent years, driven by their intriguing structural and electronic properties and the vast potential for applications. To date, ACMs have been mainly synthesized by chemical vapor deposition methods. Here, we present an alternative bottom-up synthesis approach and demonstrate the formation of a B_3N_3-substituted amorphous carbon monolayer (B_3N_3-ACM), thus introducing multiple dopant heteroatoms. In particular, we follow an ultrahigh-vacuum-based on-surface synthesis strategy by using a tailored B_3N_3-functionalized precursor to achieve uniform, large-area B_3N_3-ACMs. The characterization of the on-surface reaction products via low-temperature scanning tunneling microscopy and noncontact atomic force microscopy provides insight into their structure at the atomic scale. The covalent monolayers, formed upon thermal activation of the precursors at high coverage, were transferred onto Si/SiO_2 and a transmission electron microscope grid. Atomically-resolved electron microscope imaging combined with Raman spectroscopy confirmed the freestanding, amorphous monolayer structure of the material, incorporating nanocrystallites in disordered areas. X-ray photoelectron spectroscopy proved the presence of B and N in the 2D material after the transfer. Our on-surface synthesis protocol, combined with the demonstrated transfer abilities, showcases the potential for producing tailored heteroatom-doped amorphous materials using custom-designed molecular precursors and integrating such complex 2D architectures into devices.

1 | Introduction

Amorphous carbon monolayers (ACMs) were recently realized as 2D glass-like materials that comprise different, randomly arranged hexagonal and nonhexagonal carbon rings, promoting a variety of bond lengths and bond angles [1–3]. Their remarkable physical properties include excellent thermal stability, high breaking strength, and intrinsic toughening [1, 4, 5]. The electrical conductivity and the local electronic structure can be tuned by controlling the degree of disorder [2, 6–8], often yielding insulating behavior [1].

Birce Sena Tömekçe and Vladimir Calvi contributed equally to this work.

To date, ACMs have been synthesized primarily by conventional [2, 5, 9] and laser-assisted chemical vapor deposition (CVD), resulting in uniform layers at a large scale [1]. Alternatively, 2D amorphous carbon was achieved by conversion of graphene via electron irradiation in a transmission electron microscope (TEM) [10]. As intermediates on the amorphization trajectory [11] from perfectly crystalline graphene to ACMs, homogeneous defective graphene films [12] and nanocrystalline graphene [13] were reported, produced by a one-step CVD method with topological precursors and an irradiative and thermal treatment of self-assembled monolayers, respectively. Furthermore, several studies achieved ultrathin amorphous carbon films and membranes by solution-based deposition and annealing of carbon scaffolds, including carbon dots, polycyclic aromatic hydrocarbons, and fullerenes [14–16]. Such disordered carbon films, including defects and amorphous patches, and ACMs in particular, are promising for a broad range of applications, including magnetic recording devices, flexible electronics, sensors, active layers, dielectric layers, diffusion barriers, and nanomembranes [1, 14–18]. In this respect, amorphous monolayer materials incorporating elements beyond carbon open new perspectives. Hereby, boron (B) and nitrogen (N) attract considerable interest, complementing carbon (C) [19]. Theoretical work on N-doped monolayer amorphous carbon has shown that heteroatom incorporation can strongly reshape the electronic density of states and optical response while largely preserving the in-plane stiffness of the amorphous network [20]. N-doped ACMs have recently been realized by CVD [9] and solution-based synthesis [3]. BN incorporation is predicted to enhance the thermoelectric properties and increase the Seebeck coefficient in graphene-like carbon sheets [21, 22]. Furthermore, CVD-based amorphous boron nitride (BN) and amorphous BNC films were reported to be highly promising as dielectric materials [23, 24]. For example, amorphous BN was proven to exhibit an ultralow dielectric constant, serving as an interconnect isolation material for high-performance electronics [25].

CVD-like synthesis approaches in ultrahigh vacuum (UHV) have also been widely applied to achieve graphenic hybrid hexagonal BNC monolayers on metallic supports [26–31]. For example, temperature-induced graphenization of hexaphenyl- [32] and hexamethyl-borazine [31] was reported on Pt(111) and Ir(111), respectively. The high temperatures usually involved in the decomposition of the precursors and graphenoid formation might induce dopant and atom loss, often limiting structural order. As an alternative bottom-up approach, the on-surface synthesis strategy can provide atomic-scale control in B- and N-doped carbon nanostructures [33–35]. So far, a variety of B_3N_3-substituted nanographenes have been achieved and characterized on metallic surfaces [36–41] and a B_3N_3-containing single-layer 2D covalent porous network was synthesized on Ag(111) [42]. Only recently, a random covalent B_3N_3-substituted carbon network was achieved on Ag(111) by some of the authors of this study, employing a halogenated functionalized borazine precursor [43] and an B_3N_3-doped thin amorphous carbon film was synthesized by photopolymerization and annealing of a solution-deposited thiol-terminated borazine on a Cu foil [44]. The latter study also indicated the potential of applying transfer protocols for applications of BNC materials. Indeed, for on-surface synthesized pure carbon nanomaterials, such as graphene nanoribbons [45–48] and nanoporous graphene [49–51], distinct transfer methodologies have been developed and successfully demonstrated for device integration and further characterization on selected target substrates.

Overall, the results summarized above indicate that topology (disorder) and chemistry (heteroatom content) are two largely independent design parameters in 2D amorphous materials. Herein, we report the fabrication of B_3N_3-doped ACM (B_3N_3-ACM) and thus extend the design space by combining a disordered carbon network with a controlled density of B_3N_3, following a nanoarchitectonics approach [52]. We apply surface-assisted dehydrogenative coupling on metal substrates, using a novel functionalized borazine precursor [53]: B,B′,B″-tri (pyren-2-yl)-N,N′,N″-triphenyl borazine (in short referred to as pyrene-B_3N_3). This precursor not only provides a B_3N_3 core, but was designed containing pyrenyl moieties. These nanographene building blocks increase the precursor's molecular weight, carbon content, and stability, reducing desorption during thermal treatment and improving the formation of carbon-rich layers. We first provide insight into the temperature-induced cyclodehydrogenation reaction of pyrene-B_3N_3 on Au(111) and show the atomic structure of the resulting individual, planarized molecules by bond-resolved atomic force microscopy (AFM). Random, intermolecular C—C coupling of these intermediates at high surface coverage and elevated temperature yields densely-packed covalent networks on Au(111) and Cu(111) films, as shown by low-temperature scanning tunneling microscopy (LT-STM). Subsequently, the material was transferred onto Si/SiO_2. High-resolution TEM (HR-TEM) reveals a freestanding, extended, covalently bonded monolayer. As shown by atomic-resolution images, this monolayer is formed by nanocrystalline domains, embedded in a random carbon network, composed of 5-, 6-, 7-, and 8-membered rings. Raman spectroscopy analysis on Si/SiO_2 confirms the presence of amorphous carbon areas and nanocrystalline domains. The presence of B and N was proven by X-ray photoelectron spectroscopy (XPS). Our results thus demonstrate the bottom-up surface-assisted synthesis and successful transfer of intact and uniform B_3N_3-ACMs at the millimeter scale.

2 | Results and Discussion

Figure 1a–c schematically show the on-surface reaction sequence, from the BN-substituted precursor (Figure 1a), via planarized intermediates (Figure 1b), to the covalently coupled amorphous networks (Figure 1c). Corresponding scanning probe microscopy data of the relevant structures on Au(111) are shown in Figure 1d–g. The unreacted molecules deposited onto the substrate, kept at room temperature, feature a nonplanar configuration and typically self-assemble into tetramers. Monomers and dimers are also observed, as shown in Figure 1e. Molecular models of the precursor were overlaid on the images, e.g., confirming the tetramer-nature of the square-type agglomerates (see Figure 1e). The comparison reveals that the dim protrusions on the monomer and at the periphery of the structures can be assigned to the tilted phenyl rings adjacent to the B_3N_3 core, while the bright central protrusion of tetramers can be assigned to four pyrene units, tilted out of the surface plane, stabilizing the assembly. Lateral manipulation by the STM tip was used to disassemble the agglomerates, demonstrating that tetramers are formed from four intact precursors (see Figure S1). Annealing the substrate at

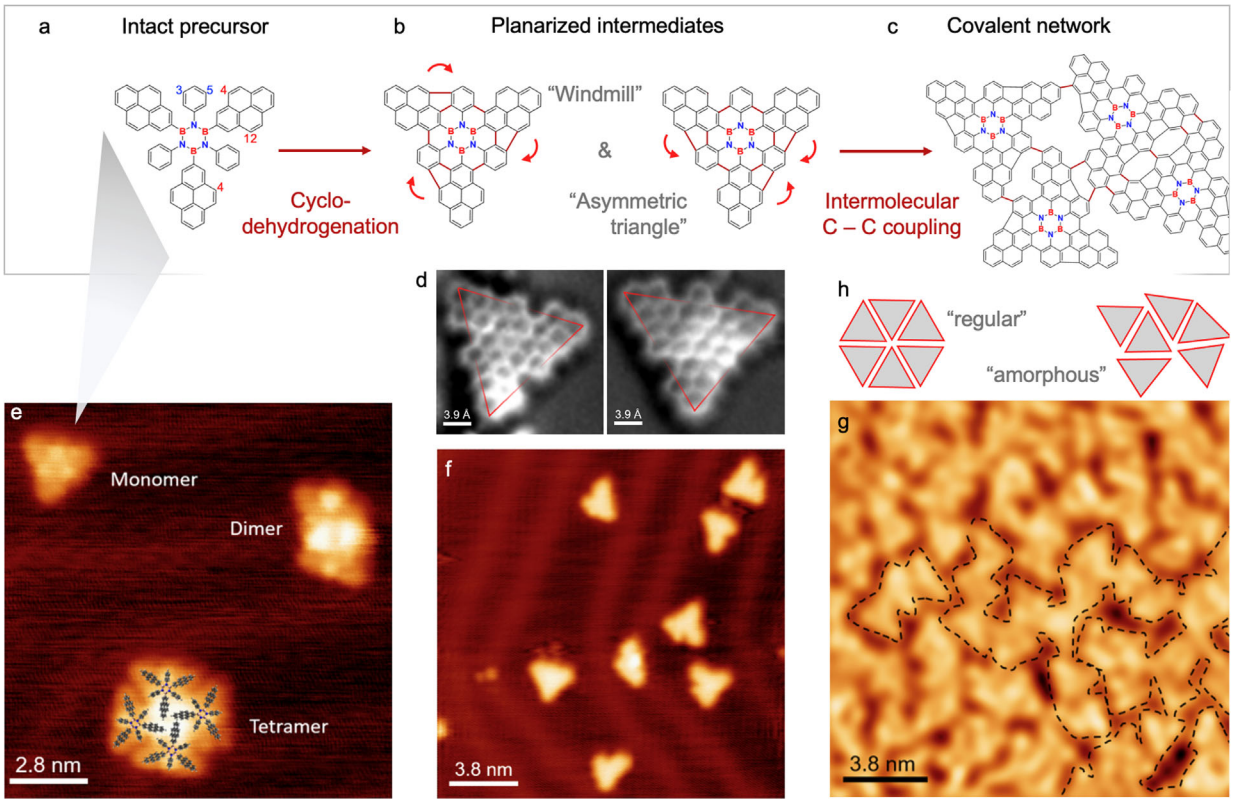

FIGURE 1 | On-surface reactions, selected intermediates, and products of pyrene-B_3N_3 on Au(111). (a–c) Reaction scheme showing the chemical structures of the unreacted precursor (a), the cyclodehydrogenated intermediates (b), and the final intermolecularly coupled network (c), respectively. The numbers in (a) mark specific carbon positions on the phenyl and pyrene moieties that can engage in bond formation. Red lines (in b,c) highlight newly formed bonds. Curved arrows illustrate the pyrene reorientation upon pentagon formation. Note that (c) only represents a schematic sketch, with the precise bonding structure elusive to the experimental characterization. (d) Bond-resolved noncontact (NC) AFM images of cyclodehydrogenated molecules, corresponding to the structural models shown above in (b). STM images of (e) the unreacted molecules (I: 48 pA, V: 1 V), (f) cyclodehydrogenated molecules (I: 70 pA, V: 0.5 V), and (g) covalent network (I: 43 pA, V: 1 V). (h) Scheme highlighting a regular structure emerging from equilateral triangles (left) in comparison to an "amorphous" structure constituted by different, coexisting (asymmetric) triangular units (right).

380°C induces cyclodehydrogenation, leading to planar species by fusion of the phenyl and pyrene groups. These species were identified by bond-resolved AFM imaging, using a CO-functionalized tip [54]. In addition to the six-membered rings surrounding the B_3N_3 cores, five-membered rings are formed next to the phenyl rings. Specifically, additional C—C bonds occur between 3 and/or 5 positions of the phenyl and 4 and/or 12 positions of the pyrene. Depending on the location of the newly formed C—C bonds constituting the pentagons and the concomitant slight reorientation of the pyrenes (see curved arrows in Figure 1b), we label these intermediates as either "windmill" or "asymmetric triangle". The "windmill" structure occurs in two chiralities (the left panels in Figure 1b,d reflect the "clockwise" chirality). The three terminal C in the pyrene moieties form a symmetric triangle, in contrast to the asymmetric triangle (right panels in Figure 1b,d). An STM image of the cyclodehydrogenated molecules is shown in Figure 1f. Further annealing at 435°C induces dehydrogenative intermolecular coupling yielding randomly fused oligomers in case of low coverage. In the case of high coverage, aiming for a B_3N_3-ACM, planarized monomers and oligomers start to merge, forming a rather dense covalent network (Figure 1g). The disorder in the network is induced by the nonselective coupling and the structural diversity of the coexisting reaction intermediates. The different edge structures (see Figure 1b,d) and alignments contribute to the amorphous character (vide infra). Figure 1h schematically contrasts such an amorphous morphology with a regular one. Even in the network structure, the STM data reveal triangle-like subunits, i.e., building blocks reflecting the planarized intermediates (Figure 1g). This assignment also reveals that the central structure including the B_3N_3 cores can be preserved in the covalent film, in line with recent findings for the on-surface synthesis of a random covalent B_3N_3-substituted carbon network from a halogenated borazine precursor [43].

In order to synthesize a B_3N_3-ACM for subsequent transfer onto Si/SiO_2 supports, we extended the same dehydrogenative intermolecular coupling strategy to $Cu(111)/Al_2O_3$ substrates. These substrates are composed of a thin copper film with a (111) termination on a sapphire substrate [55]. Figure 2a,b show sample preparations with precursor deposition for 20 and 30 min, respectively. Both samples were annealed at around 400°C to induce intermolecular coupling. To preserve the chemical structure of the molecules, particularly keeping the B_3N_3 units intact, we avoided annealing to higher temperatures. For the sample resulting from the shorter deposition time, (Figure 2a), small areas exposing the bare substrate are still discernible within the covalent network. A close-up STM image from the same sample shows the randomly-fused oligomeric networks extending over two substrate terraces (Figure 2c). A line profile, as indicated

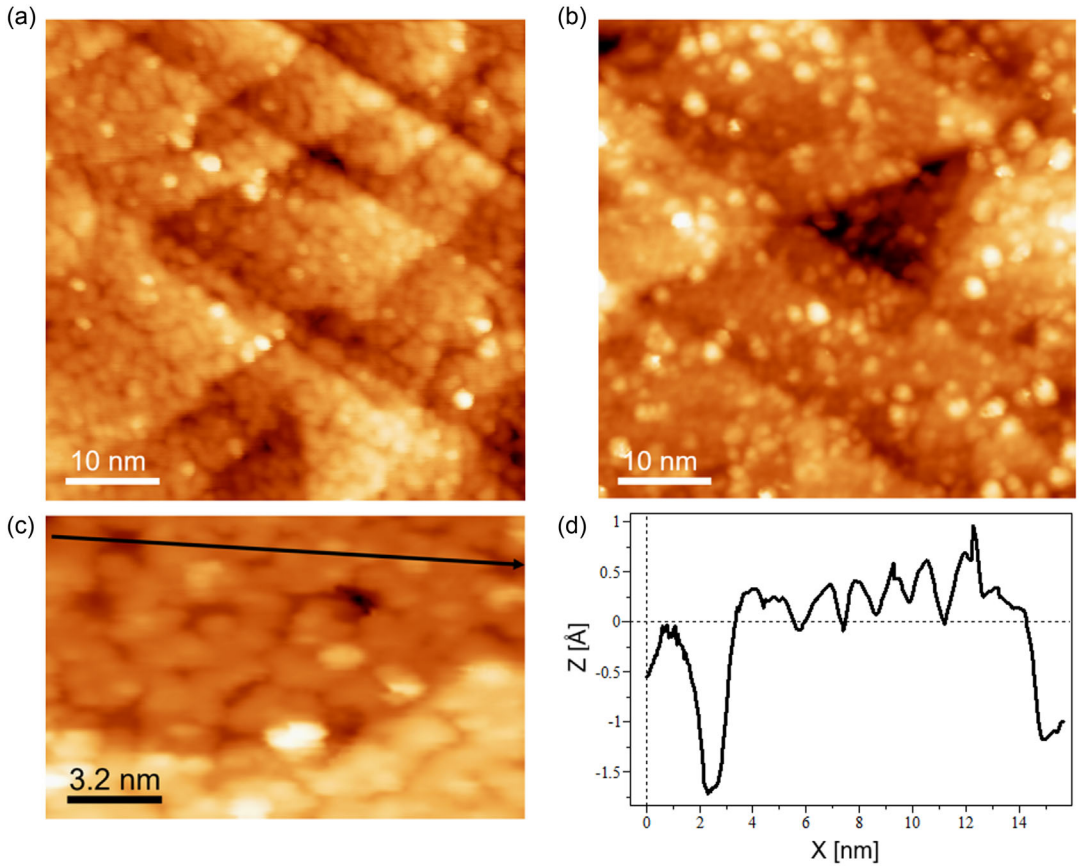

FIGURE 2 | B_3N_3-ACM on Cu(111)/Al_2O_3. STM images of the samples with (a) 20 min (I: 100 pA, V: 1 V) and (b) 30 min of precursor deposition (I: 100 pA, V: −1 V). (c) Close-up STM image taken from the lower-coverage sample, highlighting the covalent network. (I: 100 pA, V: 0.4 V). (d) Line profile taken along the black line in (c) showing the height modulation of the covalent network with reference to the substrate.

in the STM image, is presented in Figure 2d. It reveals an apparent height of the covalent network of around 1.5 Å with respect to the substrate surface, exhibiting a structural corrugation of roughly 0.5 Å. STM images representing longer (30 min, Figure 2b) and shorter deposition times (5 and 20 min, Figure S2) demonstrate a surface coverage tunable with deposition time. Specifically, the long deposition time is used to obtain a dense-packed covalent layer, with a nominal molecular coverage exceeding one monolayer (ML). In the respective STM images, molecules and molecular clusters on the dense first layer appear as bright protrusions (Figure 2b). A large-scale STM image of the same sample as well as ambient AFM images of another >1 ML coverage sample are shown in Figure S3. These images illustrate continuity and homogeneity of the covalent monolayer on a large scale, yet highlight a triangular contrast derived from the steps and terraces of Cu(111)/Al_2O_3. The detailed composition of the covalent networks and monolayers depends on the purity of the deposited precursor material, with additional pyrene contributions being possible. Figure 1 represents a sample without an excess of pyrene moieties, whereas Figure S4 shows STM data of a sample with higher pyrene content.

After STM and AFM characterization on Cu(111)/Al_2O_3, the B_3N_3-ACMs were transferred onto Si/SiO_2 supports as described in the Experimental Section and in Figure S5. After transfer, which included etching of the Cu thin film, a comprehensive characterization was performed by optical microscopy, AFM, XPS, and Raman spectroscopy. One of the samples was transferred onto a TEM grid.

Figure 3a shows a large-scale HR-TEM image of a freestanding, B_3N_3-ACM, suspended on a TEM grid. It reveals an extended sheet-like structure with voids with dimensions of a few nanometers. Such voids were not observed before transfer (e.g. Figure 2) and we thus attribute them to the loss of small domains (that were not covalently connected to the main, extended monolayer structure) during transfer. The diffractogram pattern given in the inset shows concentric diffuse halos, verifying the material's amorphous nature on this length scale. Figure 3b shows a detailed view of the area marked by the red rectangle in Figure 3a. The image confirms the flat, monolayer character of the material and clearly reveals nanocrystalline domains with hexagonal order, reaching sizes of around 1.5–2 nm and often featuring triangle-like shapes, reminiscent of the planarized monomer units shown in Figure 1b,d. Indeed, the periodicity within the domains is about 0.26 nm, consistent with the value expected for graphene [56]. Irregular areas are observed connecting the nanocrystalline domains, as expected for the non-selective coupling mechanism and imperfectly fused monomers (cf., Figure 1c). Additional large-scale TEM images, together with atomic-scale contrast in selected areas, are presented in Figure S6.

To investigate the atomic structure, aberration-corrected scanning TEM (STEM) imaging and electron energy loss spectroscopy (EELS) were performed. Figure S7 shows atomic-resolution annular dark-field (ADF) STEM images of an amorphous area, clearly revealing disordered carbon ring structures (5-, 6-, 7-, and

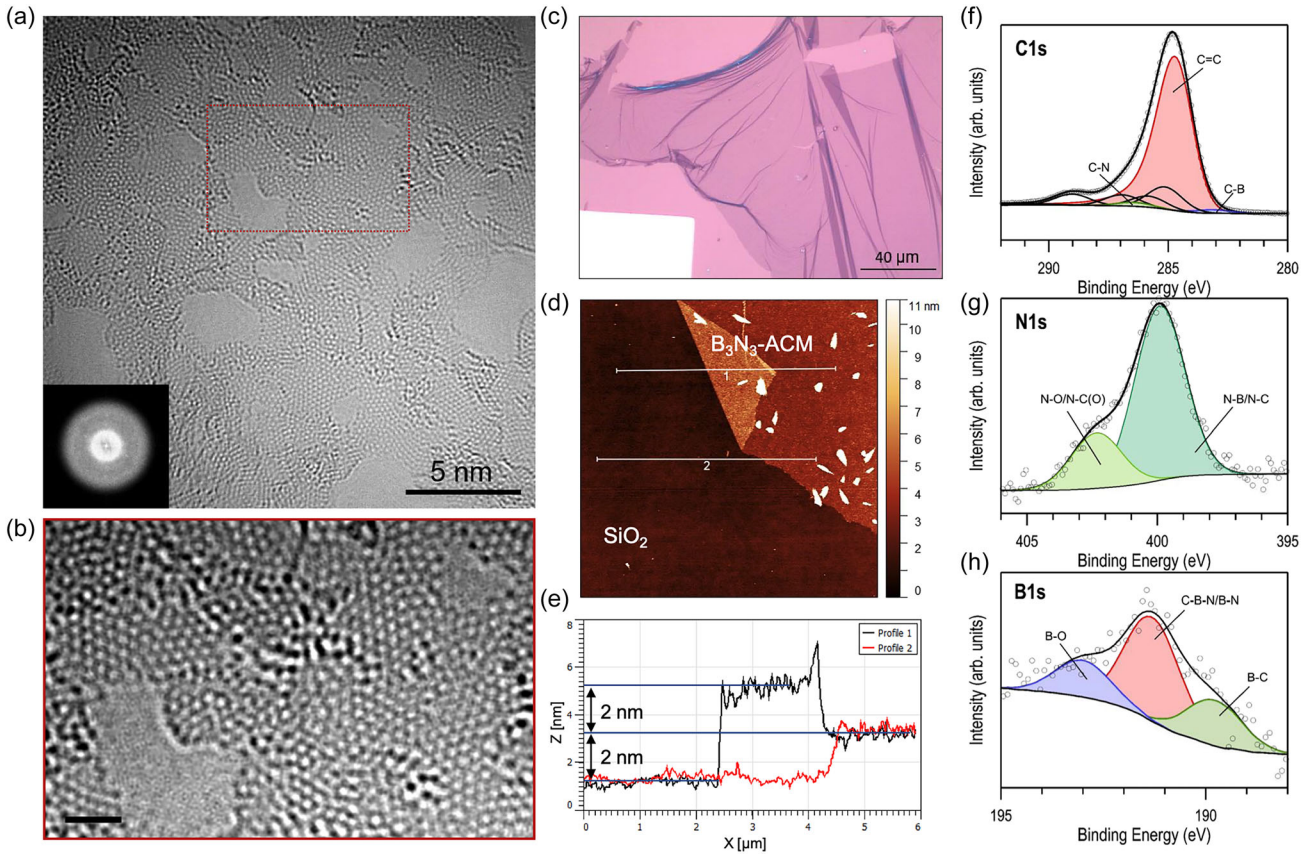

FIGURE 3 | (a) HR-TEM image obtained from one of the B_3N_3-ACM samples, freestanding on a TEM grid. Inset: Diffractogram of the image. (b) Enlarged image taken from the area indicated with a red rectangle in (a). Scale bar: 1 nm. (c) Representative optical microscopy image of B_3N_3-ACM on Si/SiO_2. Additional images are displayed in Figure S8. (d) AFM image of a folded B_3N_3-ACM (image size: $8 \times 8\ \mu m^2$) and (e) the corresponding height profiles. XPS (f) C 1s, (g) N 1s, and (h) B 1s core level spectra measured from B_3N_3-ACM on Si/SiO_2.

8-membered rings). Within the amorphous carbon network, variations in atomic column intensities suggest the incorporation of heteroatoms into the lattice. EELS spectra acquired from the same region exhibit notable features near the N–K edge, indicating the presence of nitrogen. In contrast, the B–K edge signal is less distinct, likely due to the instrumental detection limit. Consequently, for the identification of B and N in the B_3N_3-ACM, we will further rely on XPS (vide infra). Importantly, the high-resolution electron microscopy data demonstrate the chemical stability of B_3N_3-ACM after storage under atmospheric conditions for 6–8 months.

The optical microscopy images of B_3N_3-ACM on Si/SiO_2 show wrinkles and foldings, which are attributed to the transfer process, as well as extended areas with uniform contrast (Figure 3c). Additional optical microscopy images of different samples transferred onto Si/SiO_2 are provided in Figure S8. All samples possess similar homogeneity and uniformity, and no other topological features related to the intrinsic features of the monolayers are observed. Figure 3d shows an AFM image of B_3N_3-ACM with a folded edge on bare Si/SiO_2. This AFM image was taken after the sample exposure to the ambient environment, and therefore presents some contamination (white spots), attributed to dust particles. The line profiles reveal an apparent thickness of the monolayer of approximately 2 nm (Figure 3e). This value is in agreement with the value reported for a transferred nanoporous graphene film [50], but exceeds the height measured on the $Cu(111)/Al_2O_3$ substrate before transfer. We attribute this difference to the presence of poly(methyl methacrylate) (PMMA) residues, as it was shown that these residues contribute to the thickness of the layers significantly, due to resistance to removal [57, 58]. More AFM and scanning electron microscopy (SEM) images are presented in Figure S9.

XPS was performed on the B_3N_3-ACM film after transfer onto Si/SiO_2 substrates. As expected from the B_3N_3-ACM composition, C, B, and N signals are clearly observed. C 1s spectra (Figure 3f) are dominated by a main component at 284.7 eV assigned to C═C bonds (fit highlighted in red). Additional contributions at 283.1 and 286.4 eV are attributed to C—B (fit highlighted in blue) and C—N (fit highlighted in green), respectively, with minor higher-binding-energy components associated with carbonyl and carboxyl/ester groups. With the XPS measurements taken after prolonged air exposure of the sample, adventitious carbon is expected to contribute as well [59]. The N 1s signal, see Figure 3g, can be described by two broad components: a main peak at 399.9 eV corresponding to N atoms bonded to B and/or C in the doped carbon matrix and a higher-binding-energy contribution at 402.3 eV assigned to oxidized nitrogen species (N—O/N—C(O)). The B 1s region, see Figure 3h, exhibits three components. The one at 191.4 eV is consistent with B—N/B—N—C environments, 189.8 eV corresponds to B—C bonds, and 193.4 eV is attributed to oxidized boron species. A survey spectrum and a quantitative analysis with reference to literature are presented and discussed in the Supporting Information (Figure S10,

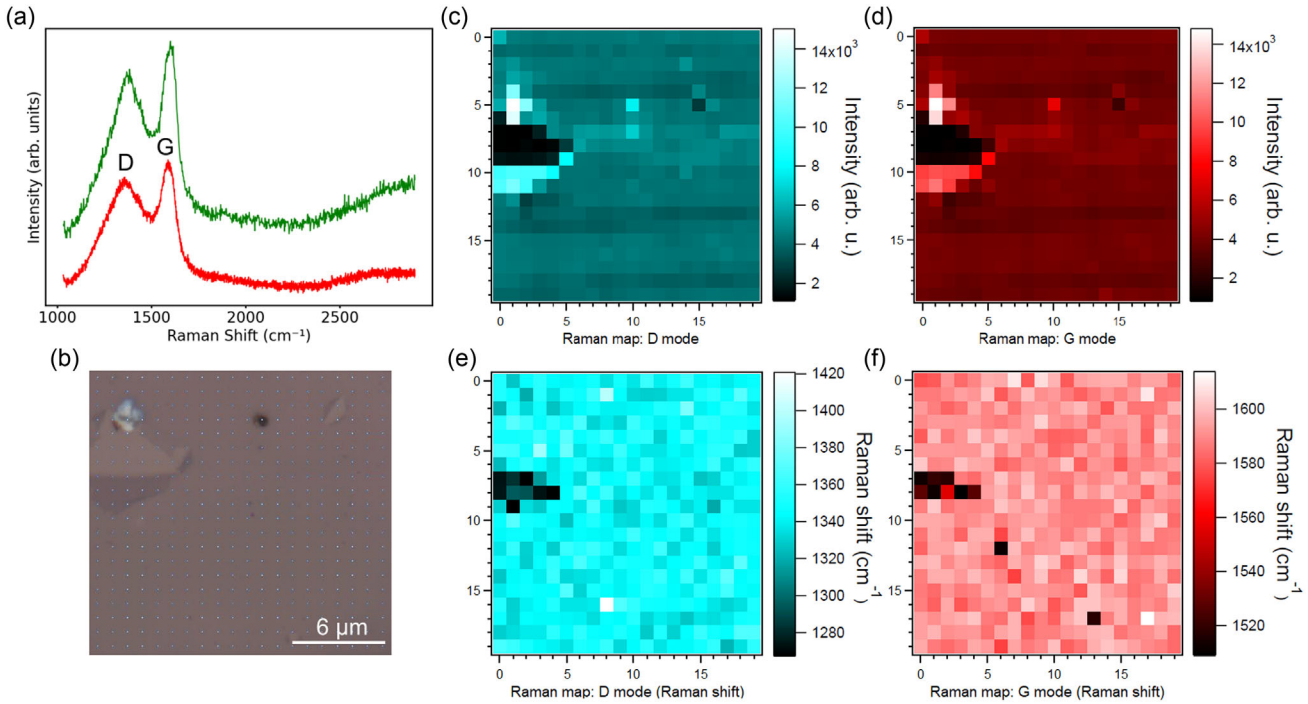

FIGURE 4 | (a) Raman spectra of B_3N_3-ACM, obtained by using a green and a red laser with wavelengths of 532 and 633 nm, respectively. (b) Optical microscopy image of an area with a folding feature and the 20×20 µm grid map. (c,d) Raman intensity maps of the D and G modes, respectively. (e,f) Raman maps illustrating the shift of the D and G modes, respectively. The I_D/I_G intensity ratio, excluding the bare SiO_2 region, is 1.07 ± 0.02, reflecting homogeneity (variation of 1.9%). Further Raman data from additional B_3N_3-ACM samples are shown in Figures S11 and S12.

Tables S1–S4), revealing a considerable contribution from the substrate (Si 13.3 and O 44.8 at.%). The combined signal from C, B, and N accounts for 40.3 at.% of the total composition and consists of 39 at.% C, 0.8 at.% N, and 0.5 at.% B, corresponding to approximately 2 at.% N and 1 at.% B relative to C. These values deviate from the ratios expected for an intrinsic B_3N_3-ACM (compare Figure 1; C:B:N 22:1:1) as PMMA, used for transfer, considerably contributes to the C signal. Nonetheless, within the experimental accuracy, the XPS data are consistent with the expected 1:1 stoichiometry of B and N in B_3N_3 and confirm the incorporation of both B and N into the C framework, with doping levels in the low atomic-percent range.

As shown in the characteristic Raman spectrum (Figure 4a) representing a randomly selected position, B_3N_3-ACM has broad and prominent D (defect-induced) and G bands, located at 1357 and 1594 cm^{-1}, respectively, measured with 633 nm (red laser). With the excitation wavelength being 532 nm (green laser), we observe the peaks being shifted to 1375 cm^{-1} for the D band and 1600 cm^{-1} for the G band due to the use of different excitation wavelengths [60, 61]. The line shapes and intensities of these bands are in close agreement with monolayer amorphous carbon [1, 2, 5, 13, 14, 18]. Note that in B_3N_3-ACM the G′ (2D) band does not appear as the sharp and intense peak characteristic of defect-free graphene. Instead, a very broad and weak feature is observed around 2800 cm^{-1}, which is consistent with the presence of nanocrystalline graphene-like domains embedded in an amorphous carbon matrix [5, 13, 18]. To demonstrate the spatial uniformity of the monolayers, Raman mapping was performed on a 20×20 point grid by using a red laser with 633 nm wavelength on a 400 μm^2 area including a torn and folded flake and bare SiO_2 (see Figure 4b). Intensity maps for the D and G modes show a rather homogeneous distribution over the single layer, while on the folded flake (bilayer) a higher signal intensity was detected (Figure 4c,d). On bare SiO_2, no signal was detected as expected. Figure 4e,f show Raman shift maps for the D and G modes, respectively, measured in the same area. The D and G modes are averaged at 1344 ± 15 and 1589 ± 12 cm^{-1}, respectively. Both modes exhibit relatively low standard deviations, even with bare SiO_2 included. No significant deviation in Raman shift was observed on the folded flake. Further Raman maps obtained from different samples can be found in Figures S11 and S12. Thermal Raman measurements were performed to investigate the thermostability of the material. Starting from room temperature, spectra were acquired at 350, 400, and 500 K (see Figure S13). During cooling, a measurement was repeated at 400 K. In all spectra, the line shapes and intensities of the D and G peaks were maintained, implying that the material did not degrade.

3 | Conclusion

In this work, we have presented the synthesis of a B_3N_3-ACM by a versatile bottom-up approach that uses a functionalized borazine precursor on various metal surfaces. Our extensive multimethod characterization after transfer onto Si/SiO_2 and a TEM grid has proven the stable monolayer nature of this new 2D material. At the nanoscale, amorphous regions coexist with crystalline domains, while optical microscopy analysis shows uniformity and homogeneity of the B_3N_3-substituted sheet on macroscopic length scales. Our UHV-based on-surface synthesis protocol thus showcases the feasibility of producing tailored, heteroatom-doped 2D materials by leveraging the precise design of molecular

precursors. In particular, our findings suggest that the B_3N_3 density and the extension of the nanographene domains embedded in amorphous carbon can be engineered. Furthermore, we demonstrate the successful transfer of such a complex architecture from a metallic substrate to distinct target supports, enabling future use in devices for further characterization and applications. The robustness, transferability, and B_3N_3-tunable nature of B_3N_3-ACMs render them highly promising materials for ultrathin dielectric and diffusion-barrier layers in 2D heterostructures, thermoelectrics, as well as for mechanically stable nanomembranes and interfacial layers in electronic and sensing devices.

4 | Experimental Section

4.1 | Molecular Synthesis and Design

The synthesis procedure of pyrene-B_3N_3 is described in the Supporting Information (see Figures S15–S19).

4.2 | Sample Preparation

Preparation of a thin film of Cu(111) on a commercially available C-plane (0001) sapphire (Al_2O_3) was as follows: Sputtering of Cu films was done in the Trikon Sigma 200 sputtering tool by preheating the sapphire substrate at 80°C and subsequent sputtering of a 2 µm-thick copper layer. Subsequently, the wafers were cooled down naturally and annealed in a separate tool at 1000°C in a 10^{-6} mbar H_2/Ar 1:2 gas mixture [62, 63]. The Cu(111)/Al_2O_3 wafer was cut with a VT07-SD320-VC100-75 disco blade in the final sample shape with dimensions of $6 \times 8\ mm^2$. The Au(111) single crystal and Cu(111)/Al_2O_3 were cleaned in UHV systems by repeated cycles of argon ion (Ar^+) sputtering. We annealed the substrate at 950°C and 10^{-4} mbar of pressure in a mixture of H_2/Ar at 1:2 ratio. The pyrene-B_3N_3 precursor was sublimated at 350°C from quartz crucibles onto clean substrates, kept at room temperature.

4.3 | STM Characterization

STM measurements were performed in two different UHV systems. Data for on-surface reaction products on Au(111) were acquired using a Createc LT-STM operating at ≈7 K with a chamber base pressure of 5×10^{-10} mbar. Experiments using Cu(111)/Al_2O_3 substrates were conducted in a chamber equipped with a Joule-Thomson STM (JT-STM, Specs) with a base pressure of 6×10^{-11} mbar operating at ≈5 K. Sample preparations were done in situ in both chambers.

4.4 | NC-AFM Imaging

For NC-AFM measurements, a Createc STM/AFM instrument equipped with a qplus sensor was used at 5 K, in a UHV chamber with a base pressure of around 1×10^{-10} mbar. The tip was CO-functionalized allowing for bond resolution. Imaging was done at constant height (z feedback off) by applying 0 bias voltage and recording the frequency shift (oscillation amplitude: 60 pm, resonance frequency: 30 kHz). The STM/AFM images were processed using the WSxM software [64].

4.5 | Ambient AFM Imaging

AFM images were acquired on a Bruker Dimension FastScan AFM operated in tapping mode (ScanAsyst mode) using ScanAsyst-Air tips. The scan size was set to 30 μm^2 with an aspect ratio of 1 and a scan rate of approximately 0.99 Hz. The images were collected with 512 lines per scan. A PeakForce amplitude of 150 nm and a PeakForce frequency of 2 kHz were used, with a lift height of ≈61 nm and a setpoint force of ≈140 pN to minimize sample damage. The cantilever had a nominal spring constant of 0.25 N/m. Images were processed and analyzed using Gwyddion software.

4.6 | Transfer onto Si/SiO_2

Before each transfer, the Si/SiO_2 with 90 nm of oxide thickness, was pretreated with O_2 plasma etching at 400 W of radio frequency (RF) power for 240 s. We performed a polymer-assisted transfer using PMMA, and chemical etching with commercially available iron chloride copper etchant was done subsequently. To avoid the PMMA remaining attached to the edges of the sapphire after the copper has been etched, Kapton tape is applied. A more detailed process diagram is illustrated in Figure S5.

4.7 | TEM, EELS Characterization

For the high-magnification TEM imaging and EELS measurements, we utilized a JEM-ARM200F at 80 kV acceleration voltage. Transfer of the monolayer was performed onto QUANTFOIL R 1.2/1.3 grid : Cu 200. The transfer onto the TEM grids was performed by using PMMA-assisted transfer with electrochemical delamination. The residues were cleaned by CO_2 at the critical point.

4.8 | Raman Spectroscopy Characterization

For Raman maps, spectra in the range of 500–3200 cm^{-1} were collected with an 800 mm focal length spectrograph (LabRAM HR, Horiba Scientific), and 600 grooves/cm blazed grating. A He–Ne laser (Thorlabs, polarized 500:1) with a wavelength of 632.817 nm was used; the laser power was ∼2 mW and the focus spot about 1 µm, objective 100x, numerical aperture (NA) = 0.95. Each spectrum was the average of 2 scans collected at 20 s. The spectra were treated using the LabSpec 6 spectroscopy suit, version 6.5.2.11. Other sets of Raman spectra were taken using a home-built system with a 532 nm laser (green laser), with the grating at 600 grooves/mm and a CCD detector model iDus 420. All spectra were referenced to the Si peak at 520 cm^{-1}.

4.9 | XPS Measurements

XPS experiments were performed on a SSX-100/206 photoelectron spectrometer (Surface Science Instruments, USA) equipped with a monochromatized microfocused Al X-ray source (powered at 10 kV and 20 mA), a 30° solid angle acceptance lens, a hemispherical analyzer, and a channel plate detector. The samples were pressed into clean stainless steel troughs of 6 mm diameter and placed on a ceramic carousel. The samples were degassed inside the sample introduction chamber overnight and transferred to the analysis chamber, where the pressure was around 10^{-8} mbar. The angle between the surface normal and the axis of

the analyzer lens was 55°. The pass energy was set at 50 eV. Under these conditions, the full width at half maximum (FWHM) of the Au $4f_{7/2}$ peak of a clean gold standard sample was around 1.1 eV. Charging effects were stabilized using a flood gun set at 8 eV and a fine-meshed Ni grid placed 1 mm above the sample surface. Peak decomposition was performed with CasaXPS processing software (Casa Software Ltd., Teignmouth, UK). The C 1s spectrum was decomposed with the least-squares fitting routine provided by the software with a Gaussian/Lorentzian (85/15) product function and after subtracting a nonlinear Shirley baseline.

4.10 | SEM Imaging

SEM images were taken on a Hitachi Regulus 8230 microscope. The acceleration voltage was set at 1 kV.

4.11 | Electrical Characterization

To perform the current–voltage (I–V) and resistance measurements, we utilized the Cascade Summit 12 000 probe station in two or four probes mode. Measurements were performed at room temperature by using high-resolution source measure units (HRSMUs).

4.12 | Statistical Analysis

Raman spectra were preprocessed by cosmic ray removal, baseline correction, and normalized to the Si peak at 520 cm^{-1} before peak fitting and quantitative analysis. For Raman maps, each map consisted of a 20×20 grid ($n = 400$ spectra per map). Peak positions and intensities of the D and G bands were obtained from fitting using a pseudo-Voigt function. Raman data are reported and coupled with mean ± standard deviation (SD). For each map, the average values and SD were calculated over all valid pixels. For temperature-dependent Raman measurements, at least three spectra were collected at different positions per temperature ($n = 3$ accumulations for each temperature point). The present work focuses on descriptive statistics; no formal hypothesis testing (e.g., t-tests, ANOVA) or p-value based inference was applied. Raman spectra and peak fitting were processed using LabSpec 6 (Horiba Scientific) and/or OriginPro (OriginLab).

Author Contributions

Birce Sena Tömekçe: formal analysis (equal), investigation (equal), writing – original draft (lead). **Vladimir Calvi**: formal analysis (equal), investigation (equal), writing – original draft (supporting). **Diego Jaramillo**: formal analysis (supporting), investigation (supporting). **Hang Sik Kim**: formal analysis (supporting), investigation (supporting). **Hyeongjoon Kim**: formal analysis (supporting), investigation (supporting). **Daniele Poletto**: formal analysis (supporting), investigation (supporting). **Vivek Chandrakant Wakchaure**: formal analysis (supporting), investigation (supporting). **Matthew David Barnes**: methodology (supporting), supervision (supporting). **Michele Buscema**: methodology (supporting), supervision (supporting). **Sorin Melinte**: funding acquisition (equal), methodology (supporting), projectadministration (supporting), supervision (equal). **Young-Min Kim**: project administration (supporting), resources (equal), supervision (equal). **Hyeon Suk Shin**: methodology (equal), project administration (supporting), resources (equal), supervision (equal). **Davide Bonifazi**: conceptualization (equal), funding acquisition (lead), supervision (equal), writing – review & editing (supporting). **Richard van Rijn**: conceptualization (supporting), methodology (equal), project administration (supporting), supervision (equal). **Irene M. N. Groot**: conceptualization (equal), funding acquisition (equal), supervision (equal), writing – review & editing (supporting). **Willi Auwärter**: conceptualization (equal), funding acquisition (equal), supervision (equal), writing – review & editing (lead).

Acknowledgments

B.S.T., V.C., and D.J. acknowledge funding from the European Union's Horizon 2020 research and innovation program under the Marie Skłodowska-Curie grant agreement No 956923 – StiBNite. H.K., Y.-M.K., and H.S.S. acknowledge support from the Institute for Basic Science (IBS-R036-D1). D.B. and V.C.W. thank the University of Vienna for the generous funding and for V.C.W.'s postdoctoral position. B.S.T. gratefully acknowledges Patrick Lawes, Mohammadreza Rostami, and Pengfei Zhao for their technical assistance during STM measurements. The authors thank Federica Saitta for the support in SEM imaging and Pierre Eloy for the XPS measurements and peak-fitting. V.C. also thanks Kaj Dockx and Daan Bijl for electrical measurements.

Funding

This work was supported by the Horizon 2020 Framework Programme (956923).

Conflicts of Interest

The authors declare no conflicts of interest

Data Availability Statement

The data that support the findings of this study are available from the corresponding author upon reasonable request.

References

1. C.-T. Toh, H. Zhang, J. Lin, et al., "Synthesis and Properties of Free-Standing Monolayer Amorphous Carbon," *Nature* 577 (2020): 199–203, https://doi.org/10.1038/s41586-019-1871-2.

2. H. Tian, Y. Ma, Z. Li, et al., "Disorder-Tuned Conductivity in Amorphous Monolayer Carbon," *Nature* 615 (2023): 56–61, https://doi.org/10.1038/s41586-022-05617-w.

3. X. Bai, P. Hu, A. Li, et al., "Nitrogen-Doped Amorphous Monolayer Carbon," *Nature* 634 (2024): 80–84, https://doi.org/10.1038/s41586-024-07958-0.

4. B. Shin, B. Ni, C.-T. Toh, et al., "Intrinsic Toughening in Monolayer Amorphous Carbon Nanocomposites," *Matter* 8 (2025): 102000, https://doi.org/10.1016/j.matt.2025.102000.

5. W.-J. Joo, J.-H. Lee, Y. Jang, et al., "Realization of Continuous Zachariasen Carbon Monolayer," *Science Advances* 3 (2017): e1601821, https://doi.org/10.1126/sciadv.1601821.

6. Y. Wang, Q. Zhang, L. Li, et al., "Turning Defects Into Advantages: Structures, Synthesis, and Applications of 2D Amorphous Carbon," *Advanced Functional Materials* 35 (2025): e09481, https://doi.org/10.1002/adfm.202509481.

7. H. Tian, Z. Yao, Z. Li, et al., "Unlocking More Potentials in Two-Dimensional Space: Disorder Engineering in Two-Dimensional Amorphous Carbon," *ACS Nano* 17 (2023): 24468–24478, https://doi.org/10.1021/acsnano.3c09593.

8. L. Shi, H. Zhang, A. K. Grebenko, et al., "Monolayer Amorphous Carbon: Unlocking Disorder-Induced Lithiophilicity," *Advanced Science* (2025): e16490, https://doi.org/10.1002/advs.202516490.

9. Z. Li, H. Tian, U. S., et al., "Polycyclic Molecule Chemical Vapor Deposition of Amorphous Monolayer Carbon," *Advanced Functional Materials* 35 (2025): 2424751, https://doi.org/10.1002/adfm.202424751.

10. J. Kotakoski, A. V. Krasheninnikov, U. Kaiser, and J. C. Meyer, "From Point Defects in Graphene to Two-Dimensional Amorphous Carbon," *Physical Review Letters* 106 (2011): 105505, https://doi.org/10.1103/physrevlett.106.105505.

11. A. C. Ferrari and J. Robertson, "Interpretation of Raman Spectra of Disordered and Amorphous Carbon," *Physical Review B* 61 (2000): 14095–14107, https://doi.org/10.1103/physrevb.61.14095.

12. B. P. Klein, M. A. Stoodley, J. Deyerling, et al., "One-Step Synthesis of Graphene Containing Topological Defects," *Chemical Science* 16 (2025): 19403–19413, https://doi.org/10.1039/d5sc03699b.

13. A. Turchanin, D. Weber, M. Büenfeld, et al., "Conversion of Self-Assembled Monolayers into Nanocrystalline Graphene: Structure and Electric Transport," *ACS Nano* 5 (2011): 3896–3904, https://doi.org/10.1021/nn200297n.

14. F. An, C. Wang, V. H. Pham, et al., "Ultrathin Quasi-2D Amorphous Carbon Dielectric Prepared from Solution Precursor for Nanoelectronics," *Communications Engineering* 2 (2023): 93, https://doi.org/10.1038/s44172-023-00141-9.

15. X. Liu, M. He, D. Calvani, et al., "Power Generation by Reverse Electrodialysis in a Single-Layer Nanoporous Membrane Made from Core–rim Polycyclic Aromatic Hydrocarbons," *Nature Nanotechnology* 15 (2020): 307–312, https://doi.org/10.1038/s41565-020-0641-5.

16. M. He, Y. Ding, and X. Liu, "Nanoporous Amorphous Carbon Monolayer Derived from Fullerene Film," *Advanced Science* 11 (2024): 2308187, https://doi.org/10.1002/advs.202308187.

17. I.-S. Kim, C.-E. Shim, S. W. Kim, et al., "Amorphous Carbon Films for Electronic Applications," *Advanced Materials* 35 (2023): e2204912, https://doi.org/10.1002/adma.202204912.

18. B.-S. An, Y. Kwon, J.-S. Oh, et al., "Characteristics of an Amorphous Carbon Layer as a Diffusion Barrier for an Advanced Copper Interconnect," *ACS Applied Materials & Interfaces* 12 (2020): 3104–3113, https://doi.org/10.1021/acsami.9b15562.

19. M. M. Lorenzo-García and D. Bonifazi, "Renaissance of an Old Topic: From Borazines to BN-Doped Nanographenes," *CHIMIA International Journal for Chemistry* 71 (2017): 550–557, https://doi.org/10.2533/chimia.2017.550.

20. E. J. A. d. Santos, M. L. Pereira, R. M. Tromer, et al., "Exploring the Electronic and Mechanical Properties of the Recently Synthesized Nitrogen-Doped Amorphous Monolayer Carbon," *Nanoscale* 17 (2025): 7253–7263, https://doi.org/10.1039/D4NR04305G.

21. N. R. Abdullah, D. A. Abdalla, T. Y. Ahmed, et al., "Effect of BN Dimers on the Stability, Electronic, and Thermal Properties of Monolayer Graphene," *Results in Physics* 18 (2020): 103282, https://doi.org/10.1016/j.rinp.2020.103282.

22. L. Caputo, V.-H. Nguyen, and J.-C. Charlier, "Thermoelectric Properties of Graphene through BN-ring Doping: A Theoretical Investigation," *Carbon* 229 (2024): 119456, https://doi.org/10.1016/j.carbon.2024.119456.

23. S. W. King, "Dielectric Barrier, Etch Stop, and Metal Capping Materials for State of the Art and beyond Metal Interconnects," *ECS Journal of Solid State Science and Technology* 4 (2015): 3029–3047, https://doi.org/10.1149/2.0051501jss.

24. E. R. Engbrecht, Y.-M. Sun, K. H. Junker, et al., "Chemical Vapor Deposition Boron Carbo–nitride Deposited Using Dimethylamine Borane with Ammonia and Ethylene," *Journal of Vacuum Science & Technology A: Vacuum Surfaces and Films* 22 (2004): 2152–2158, https://doi.org/10.1116/1.1778405.

25. S. Hong, C.-S. Lee, M.-H. Lee, et al., "Ultralow-Dielectric-Constant Amorphous Boron Nitride," *Nature* 582 (2020): 511–514, https://doi.org/10.1038/s41586-020-2375-9.

26. L. Ci, L. Song, C. Jin, et al., "Atomic Layers of Hybridized Boron Nitride and Graphene Domains," *Nature Materials* 9 (2010): 430–435, https://doi.org/10.1038/nmat2711.

27. Y. Gong, G. Shi, Z. Zhang, et al., "Direct Chemical Conversion of Graphene to Boronand Nitrogen- and Carbon-Containing Atomic Layers," *Nature Communications* 5 (2014): 3193, https://doi.org/10.1038/ncomms4193.

28. Y. Gao, Y. Zhang, P. Chen, et al., "Toward Single-Layer Uniform Hexagonal Boron Nitride–Graphene Patchworks with Zigzag Linking Edges," *Nano Letters* 13 (2013): 3439–3443, https://doi.org/10.1021/nl4021123.

29. K. A. Bokai, A. V. Tarasov, V. O. Shevelev, et al., "Hybrid h-BN–Graphene Monolayer with B–C Boundaries on a Lattice-Matched Surface," *Chemistry of Materials* 32 (2020): 1172–1181, https://doi.org/10.1021/acs.chemmater.9b04207.

30. S. Beniwal, J. Hooper, D. P. Miller, et al., "Graphene-Like Boron–Carbon–Nitrogen Monolayers," *ACS Nano* 11 (2017): 2486–2493, https://doi.org/10.1021/acsnano.6b08136.

31. N. Herrera-Reinoza, A. C. d. Santos, L. H. d. Lima, et al., "Atomically Precise Bottom-Up Synthesis of h-BNC: Graphene Doped with h-BN Nanoclusters," *Chemistry of Materials* 33 (2021): 2871–2882, https://doi.org/10.1021/acs.chemmater.1c00081.

32. G. Imamura, C. W. Chang, Y. Nabae, et al., "Electronic Structure and Graphenization of Hexaphenylborazine," *The Journal of Physical Chemistry C* 116 (2012): 16305–16310, https://doi.org/10.1021/jp304879s.

33. S. Kawai, S. Saito, S. Osumi, et al., "Atomically Controlled Substitutional Borondoping of Graphene Nanoribbons," *Nature Communications* 6 (2015): 8098, https://doi.org/10.1038/ncomms9098.

34. R. Pawlak, X. Liu, S. Ninova, et al., "Bottom-up Synthesis of Nitrogen-Doped Porous Graphene Nanoribbons," *Journal of the American Chemical Society* 142 (2020): 12568–12573, https://doi.org/10.1021/jacs.0c03946.

35. R. Pawlak, X. Liu, S. Ninova, et al., "On-Surface Synthesis of Nitrogen-Doped Kagome Graphene," *Angewandte Chemie International Edition* 60 (2021): 8370, https://doi.org/10.1002/anie.202016469.

36. M. Krieg, F. Reicherter, P. Haiss, et al., "Construction of an Internally B_3N_3 -Doped Nanographene Molecule," *Angewandte Chemie* 127, no. 28 (2015): 8402–8404, https://doi.org/10.1002/ange.201412165.

37. J. Dosso, T. Battisti, B. D.Ward, et al., "Boron–Nitrogen-Doped Nanographenes: A Synthetic Tale from Borazine Precursors," *Chemistry – A European Journal* 26 (2020): 6608–6621, https://doi.org/10.1002/chem.201905794.

38. J. Dosso, J. Tasseroul, F. Fasano, et al., "Synthesis and Optoelectronic Properties of Hexa-Peri-Hexabenzoborazinocoronene," *Angewandte Chemie International Edition* 56 (2017): 4483–4487, https://doi.org/10.1002/anie.201700907.

39. A. Belser, K. Greulich, P. Grüninger, et al., "Visualization of the Borazine Core of B3N3-Doped Nanographene by STM," *ACS Applied Materials & Interfaces* 12 (2020): 19218–19225, https://doi.org/10.1021/acsami.0c02324.

40. K. Greulich, A. Belser, D. Bischof, et al., "B3N3-Substituted Nanographene Molecules: Influence of Planarity on the Electronic Structure and Molecular Orientation in Thin Films," *ACS Applied Electronic Materials* 3 (2021): 825–837, https://doi.org/10.1021/acsaelm.0c00967.

41. A. Belser, K. Greulich, M. Klein, et al., "Planar BN-Doped Nanographenes on Reactive Metal Surfaces: A Promising Pathway for the Preparation of BN-Doped Graphene Layers," *ACS Applied Electronic Materials* 5 (2023): 5193–5201, https://doi.org/10.1021/acsaelm.3c00924.

42. C. Sánchez-Sánchez, S. Brüller, H. Sachdev, et al., "On-Surface Synthesis of BNSubstituted Heteroaromatic Networks," *ACS Nano* 9 (2015): 9228–9235, https://doi.org/10.1021/acsnano.5b03895.

43. B. S. Tömekce, M. G. Cuxart, L. Caputo, et al., "Surface Chemistry of a Halogenated Borazine: From Supramolecular Assemblies to a Random Covalent BN-Substituted Carbon Network," *Chemistry – A European Journal* 30 (2024): e202402492, https://doi.org/10.1002/chem.202402492.

44. C. M. Ibarra-Barreno, S. Chowdhury, M. Crosta, et al., "Bottom-Up Fabrication of BN-Doped Graphene Electrodes from Thiol-Terminated Borazine Molecules Working in Solar Cells," *ACS Applied Materials & Interfaces* 17 (2025): 23062–23075, https://doi.org/10.1021/acsami.4c23116.

45. Z. Chen, A. Narita, and K. Müllen, "Graphene Nanoribbons: On-Surface Synthesis and Integration into Electronic Devices," *Advanced Materials* 32 (2020): e2001893, https://doi.org/10.1002/adma.202001893.

46. G. B. Barin, A. Fairbrother, L. Rotach, et al., "Surface-Synthesized Graphene Nanoribbons for Room Temperature Switching Devices: Substrate Transfer and ex Situ Characterization," *ACS Applied Nano Materials* 2 (2019): 2184–2192, https://doi.org/10.1021/acsanm.9b00151.

47. G. B. Barin, Q. Sun, M. D. Giovannantonio, et al., "Growth Optimization and Device Integration of Narrow-Bandgap Graphene Nanoribbons," *Small* 18 (2022): e2202301, https://doi.org/10.1002/smll.202202301.

48. M. E. Abbassi, M. L. Perrin, G. B. Barin, et al., "Controlled Quantum Dot Formation in Atomically Engineered Graphene Nanoribbon Field-Effect Transistors," *ACS Nano* 14 (2020): 5754–5762, https://doi.org/10.1021/acsnano.0c00604.

49. C. Moreno, M. Vilas-Varela, B. Kretz, et al., "Bottom-up Synthesis of Multifunctional Nanoporous Graphene," *Science* 360 (2018): 199–203, https://doi.org/10.1126/science.aar2009.

50. Z. Mutlu, P. H. Jacobse, R. D. McCurdy, et al., "Bottom-Up Synthesized Nanoporous Graphene Transistors," *Advanced Functional Materials* 31 (2021): 2103798, https://doi.org/10.1002/adfm.202103798.

51. B. Lisboa, M. Soler, R. Singh, et al., "Nanoporous Graphene Integrated onto Bimodal Waveguide Biosensors for Detection of C-Reactive Protein," *ACS Applied Nano Materials* 8 (2025): 1640–1648, https://doi.org/10.1021/acsanm.4c06716.

52. K. Ariga, "Nanoarchitectonics: The Method for Everything in Materials Science," *Bulletin of the Chemical Society of Japan* 97 (2023): uoad001, https://doi.org/10.1093/bulcsj/uoad001.

53. D. Bonifazi, F. Fasano, M. M. Lorenzo-Garcia, et al., "Boron–nitrogen Doped Carbon Scaffolding: Organic Chemistry, Self-Assembly and Materials Applications of Borazine and Its Derivatives," *Chemical Communications* 51 (2015): 15222–15236, https://doi.org/10.1039/c5cc06611e.

54. L. Gross, F. Mohn, N. Moll, et al., "The Chemical Structure of a Molecule Resolved by Atomic Force Microscopy," *Science* 325 (2009): 1110–1114, https://doi.org/10.1126/science.1176210.

55. T.-A. Chen, C.-P. Chuu, C.-C. Tseng, et al., "Wafer-Scale Single-Crystal Hexagonal Boron Nitride Monolayers on Cu (111)," *Nature* 579 (2020): 219–223, https://doi.org/10.1038/s41586-020-2009-2.

56. Z. Shen, J. Li, M. Yi, X. Zhang, and S. Ma, "Preparation of Graphene by Jet Cavitation," *Nanotechnology* 22 (2011): 365306, https://doi.org/10.1088/0957-4484/22/36/365306.

57. B. Zhuang, S. Li, S. Li, et al., "Ways to Eliminate PMMA Residues on Graphene—superclean Graphene," *Carbon* 173 (2021): 609–636, https://doi.org/10.1016/j.carbon.2020.11.047.

58. R. Li, Z. Li, E. Pambou, et al., "Determination of PMMA Residues on a Chemical- Vapor-Deposited Monolayer of Graphene by Neutron Reflection and Atomic Force Microscopy," *Langmuir* 34 (2018): 1827–1833, https://doi.org/10.1021/acs.langmuir.7b03117.

59. M. C. Biesinger, "Accessing the Robustness of Adventitious Carbon for Charge Referencing (correction) Purposes in XPS Analysis: Insights from a Multi-User Facility Data Review," *Applied Surface Science* 597 (2022): 153681, https://doi.org/10.1016/j.apsusc.2022.153681.

60. A. C. Ferrari, J. C. Meyer, V. Scardaci, et al., "Raman Spectrum of Graphene and Graphene Layers," *Physical Review Letters* 97 (2006): 187401, https://doi.org/10.1103/physrevlett.97.187401.

61. L. G. Cançado, A. Jorio, E. H. M. Ferreira, et al., "Quantifying Defects in Graphene via Raman Spectroscopy at Different Excitation Energies," *Nano Letters* 11 (2011): 3190–3196, https://doi.org/10.1021/nl201432g.

62. G. Janssen, N. v. d. Pers, R. Hendrikx, et al., "Single-Crystal Copper Films on Sapphire," *Thin Solid Films* 709 (2020): 138137, https://doi.org/10.1016/j.tsf.2020.138137.

63. Y. Li, L. Sun, H. Liu, et al., "Preparation of Single-Crystal Metal Substrates for the Growth of High-Quality Two-Dimensional Materials," *Inorganic Chemistry Frontiers* 8 (2021): 182–200, https://doi.org/10.1039/d0qi00923g.

64. I. Horcas, R. Fernández, J. M. Gómez-Rodríguez, et al., "WSXM: A Software for Scanning Probe Microscopy and a Tool for Nanotechnology," *Review of Scientific Instruments* 78 (2007): 013705, https://doi.org/10.1063/1.2432410.

Supporting Information

Additional supporting information can be found online in the Supporting Information section. **Supporting Fig. S1:** STM lateral manipulation of tetramers. **Supporting Fig. S2:** Additional STM images taken on Cu(111)/Al_2O_3. **Supporting Fig. S3:** Characterization of the high-coverage samples on Cu(111)/Al_2O_3 before transfer. **Supporting Fig. S4:** STM images taken from the control experiment on Au(111) without annealing. **Supporting Fig. S5:** (a) Schematics depicting the steps of the sample preparation for transfer and chemical etching. **Supporting Fig. S6:** TEM and HR-TEM characterization of B_3N_3-ACM. **Supporting Fig. S7:** Aberration-corrected STEM-ADF and EELS characterization of B_3N_3-ACM. **Supporting Fig. S8:** Optical images of B_3N_3-ACM film before and after transfer. **Supporting Fig. S9:** AFM and SEM images. **Supporting Fig. S10:** XPS survey spectrum of B_3N_3-ACM on Si/SiO_2. **Supporting Fig. S11:** Raman mapping for sample (S02). **Supporting Fig. S12:** Raman mapping for sample (S05). **Supporting Fig. S13:** Raman spectra acquired at different temperatures. **Supporting Fig. S14:** SEM and optical microscopy images of the two-probe and FET devices, electrical measurements. **Supporting Fig. S15:** Synthesis scheme. **Supporting Fig. S16:** ^{1}H NMR spectrum of pyrene-B_3N_3 (600 MHz, CD_2Cl_2). **Supporting Fig. S17:** ^{13}C $\{^{1}H\}$ NMR spectrum of pyrene-B_3N_3 (151 MHz, CD_2Cl_2). **Supporting Fig. S18:** ^{11}B NMR spectrum of pyrene-B_3N_3 (193 MHz, CD_2Cl_2). **Supporting Fig. S19:** High-resolution mass spectrum of pyrene-B_3N_3. **Supporting Table S1:** Quantification analysis of B_3N_3-ACM on Si/SiO_2. **Supporting Table S2:** Carbon contribution in B_3N_3-ACM on Si/SiO_2. **Supporting Table S3:** Nitrogen contribution in B_3N_3-ACM on Si/SiO_2. **Supporting Table S4:** Boron contribution in B_3N_3-ACM on Si/SiO_2.